Population dynamics and entrainment of basal ganglia pacemakers are shaped by their dendritic arbors

Lior Tiroshi[1,2] and Joshua A. Goldberg[1]

[1]Department of Medical Neurobiology, Institute of Medical Research Israel – Canada, The Faculty of Medicine,

[2]Edmond and Lily Safra Center for Brain Sciences,

The Hebrew University of Jerusalem, 9112102, Jerusalem, Israel

Running Title: Collective dynamics of dendritic SNr pacemakers

Corresponding author:

Joshua A. Goldberg

Department of Medical Neurobiology

Institute of Medical Research Israel – Canada

The Faculty of Medicine

The Hebrew University of Jerusalem

POB 12272, Ein Kerem Campus

9112102 Jerusalem, Israel

E-mail: joshg@ekmd.huji.ac.il

Tel: +972-2-675-7385

Fax: +972-2-643-9736

Abstract

The theory of phase oscillators is an essential tool for understanding population dynamics of pacemaking neurons. GABAergic pacemakers in the substantia nigra pars reticulata (SNr), a main basal ganglia (BG) output nucleus, receive inputs from the direct and indirect pathways at distal and proximal regions of their dendritic arbors, respectively. We combine theory, optogenetic stimulation and electrophysiological experiments in acute brain slices to ask how dendritic properties impact the propensity of the various inputs, arriving at different locations along the dendrite, to recruit or entrain SNr pacemakers.

By combining cable theory with sinusoidally-modulated optogenetic activation of either proximal somatodendritic regions or the entire dendritic arbor of SNr neurons, we construct an analytical model that accurately predicts the empirically measured somatic current response to inputs arising from illuminating various portions of the dendritic field. We show that the extent of the dendritic tree that is illuminated generates measurable and systematic differences in the pacemaker's phase response curve (PRC), causing a shift in its peak. Finally we show that the divergent PRCs correctly predict differences in two major features of the collective dynamics of SNr neurons: the fidelity of population responses to sudden step-like changes in inputs; and the phase latency at which SNr neurons are entrained by rhythmic stimulation, which can occur in the BG under both physiological and pathophysiological conditions.

Our novel method generates measurable and physiologically meaningful spatial effects, and provides the first empirical demonstration of how the collective responses of SNr pacemakers are determined by the transmission properties of their dendrites. SNr dendrites may serve to delay distal striatal inputs so that they impinge on the spike initiation zone simultaneously with pallidal and subthalamic inputs in order to guarantee a fair competition between the influence of the monosynaptic direct- and polysynaptic indirect pathways.

Author Summary

The substantia nigra pars reticulata (SNr) is a main output nucleus of the basal ganglia (BG), where inputs from the competing direct and indirect pathways converge onto the same neurons. Interestingly, these inputs are differentially distributed with direct and indirect pathway projections arriving at distal and proximal regions of the dendritic arbor, respectively. We employ a novel method combining theory with electrophysiological experiments and optogenetics to study the distinct effects of inputs arriving at different locations along the dendrite.

Our approach represents a useful compromise between complexity and reduction in modelling. Our work addresses the question of high fidelity encoding of inputs by networks of neurons in the new context of pacemaking neurons, which are driven to fire by their intrinsic dynamics rather than by a network state. We provide the first empirical demonstration that dendritic delays can introduce latencies in the responses of a population of neurons that are commensurate with synaptic delays, suggesting a new role for SNr dendrites with implications for BG function.

Keywords: channelrhodopsin-2; synchrony; phase reduction; Rall cable theory; entrainment; nonlinear dynamics; iterative map; direct and indirect pathways; Peristimulus time histogram (PSTH); Fokker-Planck

Introduction

The basal ganglia (BG) are a collection of forebrain nuclei involved in various aspects of motor control and habit formation. The substantia nigra pars reticulata (SNr) is one of the main output nuclei of the BG, innervating the ventral thalamus, superior colliculus and reticular formation (1–3). SNr GABAergic neurons receive thousands of synaptic inputs. Most of them are inhibitory inputs arising from direct

pathway spiny projection neurons (dSPNs) in the striatum (4,5), or from the external segment of the globus pallidus (GPe) in the indirect pathway (6,7). Excitatory inputs originate from the subthalamic nucleus (STN) (8,9), the pedunculpontine nuclei (PPN) (10), and, to a lesser extent, from the cerebral cortex (11). Thus, in the SNr, inputs from the direct and indirect pathways converge onto the same neuron.

The vast majority of SNr GABAergic neurons are autonomously active and discharge continuously and regularly at 6-30 spikes/s in rodents *in vitro* (12–15), even when their synaptic inputs are completely blocked and at higher rates *in vivo* (16–18). A rhythmically firing neuron – also called a pacemaker neuron – can be represented by a phase variable that advances from 0 to 1 as the somatic voltage of the pacemaker neuron advances from one action potential threshold to the next. Such a phase oscillator is sensitive to the timing of impinging inputs. Thus, in the case of a pacemaker neuron, each individual synaptic input is sufficiently small so that its only lasting effect is a finite change in the phase of the pacemaker that either postpones or advances the next spike. The sign and amplitude of this phase change depend on the phase of the pacemaker's cycle at which the synaptic input arrived. Thus, the complex neuronal dynamics of synaptic integration by the pacemaker are reduced to phase change as a function of the timing of inputs (19–22). This reduction vastly simplifies the treatment of the collective dynamics of populations of pacemakers.

The quantity that describes the susceptibility of the pacemaker neuron's phase to small voltage perturbation as a function of the timing of the perturbation is called the neuron's phase response curve (PRC) (19–22). Although the phase reduction and the use of PRCs are theoretically valid only for weak perturbations, they prove to be very useful in practice. The PRC in response to somatic stimulations can be easily measured experimentally, and has been used successfully to predict neurons' responses to arbitrary patterns of somatic current injections (23–30). Thus, the phase reduction is computationally simple, can capture the essence of the neuronal dynamics, and can be readily implemented experimentally on real neurons.

The use of phase reductions and PRCs has been applied both experimentally and theoretically (23,24,27,29,30), by and large, only to somatic voltage perturbations. However, neurons can possess elaborate dendritic arbors. Previous theoretical and experimental work has suggested that PRCs need to be redefined and generalized to accommodate inputs arriving at the dendritic arbors (31–33). These studies predicted that taking the dendritic localization of inputs into consideration could have a measurable effect on collective neurons dynamics. Here, we put this prediction to test for the first time, and do so for actual neuronal pacemakers with dendrites.

SNr neurons in mice possess dendrites that can extend up to 0.75 mm long, usually branching only once or twice (34,35). Excitatory inputs from the STN are distributed along the entire length of the dendrites (36,37). In contrast, the two major inhibitory inputs are differentially distributed: inputs from the GPe, belonging to the indirect pathway, are located at the soma and on proximal dendrites (38–41), while direct pathway striatal synapses impinge upon smaller distal dendrites and terminal tufts (41). The functional relevance of the differential spatial organization of direct and indirect pathway inputs is unknown.

We combine theory and electrophysiological experiments in acute brain slices from transgenic mice that express channelrhodopsin-2 (Thy1-ChR2 mice) in GABAergic SNr neurons (42,43) to investigate the impact of dendritic localization of synaptic inputs on the control of spike timing in these pacemakers. This assay allows us to directly perturb the membrane voltage at various locations on the somatodendritic tree. In order to compare stimulation of proximal *vs.* distal locations on the dendritic arbor, we illuminate either a small region containing the soma and very proximal dendrites or a wider field of view containing the entire dendritic tree, while measuring somatic currents and voltage. This approach eliminates the effect of the variability arising from the shape of individual dendritic arbors and generates more robust results. Moreover, it allows us to use a simple cable theoretic model, in which the entire dendritic tree is collapsed to a single cable, to fit the experimental results.

We begin by investigating the electrotonic structure of SNr GABAergic pacemakers using periodic perturbations, and constructing a model that accurately predicts the somatic current response to inputs arising from stimulating various portions of the dendritic arbor. Next, we show that the choice of whether to illuminate only the soma and proximal dendrites or the entire dendritic arbor generates measurable and systematic differences in the PRCs corresponding to each of these conditions. Finally, we show that the divergent PRCs correctly predict differences in two major features of the collective dynamics of SNr neurons. The fidelity and latency of population responses to sudden changes in inputs, on the one hand, and the phase latency at which SNr neurons are entrained by rhythmic stimulation, on the other, are both determined by the extent of the dendritic tree illuminated – in close agreement with predictions arising from their respective empirical PRCs.

This is the first experimental demonstration of the direct impact of the electrotonic structure of the dendritic arbor on the collective dynamics of pacemaker neurons. Our results suggest a possible role for the differential spatial distribution of inputs onto SNr GABAergic neurons, where SNr dendrites may serve to delay distal striatal inputs so that they impinge on the spike initiation zone simultaneously with pallidal and subthalamic inputs. Coherent rhythmic inputs to SNr neurons arise under various physiological (e.g., sleep, (44)) and pathophysiological (e.g., parkinsonism, (18,45)) conditions. Thus, the way in which these neurons follow their inputs, or become entrained to them, will depend on the spatial distribution of their inputs throughout their dendritic arbor (e.g., distal striatal vs. proximal pallidal inputs).

Results

A cable theoretic model of optogenetic dendritic activation

In order to investigate the impact of the dendritic location of inputs on the SNr pacemakers, we employed our previously published model of a semi-infinite cable attached to a pacemaking axosomatic

compartment (32). Active dendritic conductances are incorporated into the model by linearizing them in the vicinity of the dendrite's resting membrane potential, resulting in a quasi-linear cable *u(x,t)* (Fig. 1A) whose Green's function is given by

$$G(x,t) = \int_{-\infty}^{\infty} \frac{d\omega}{2\pi} \int_{-\infty}^{\infty} \frac{dk}{2\pi} \frac{e^{i(kx+\omega t)}}{\lambda^2 k^2 + \alpha(\omega) + i\beta(\omega)}$$

Where λ is the space constant of the cable and $\alpha(\omega)$ and $\beta(\omega)$ are the contributions from the passive cable properties as well as terms that arise from linearizing the nonlinear conductances in the cable (32,33). In particular, for a linear cable $\alpha(\omega) = 1$ and $\beta(\omega) = \omega\tau$ (32), where τ is the time constant of the cable.

Because we are interested in the current injected into the soma by the cable, we assume that it is semi-infinite where the somatic boundary at $x = 0$ is kept at a constant holding potential $u(0,t) = u_0$ for all *t*. In the voltage clamp experiments this assumption is enforced experimentally. Thus, the current injected into the soma is proportional to the spatial derivative of $u(x,t)$ at $x = 0$, with a proportionality factor κ:

$$I(t) = \kappa \frac{\partial}{\partial x}\Big|_{x=0} u(x,t)$$

The Green's function for the semi-infinite (si) cable with these boundary conditions is given by

$$G_{si}(x,y,t) = G(x-y,t) - G(x+y,t)$$

The optogenetic stimulation of the cell is modeled as a band of illumination that starts at distance *r* from the soma and ends at distance *R*, where the stimulus has the temporal waveform $cos(\omega\, t)$, with $\omega = 2\pi f$ where *f* is the driving frequency. To calculate the current injected into the soma it is necessary to integrate the input from *r* to *R* and over all time. Thus,

$$I(t) = \kappa \frac{\partial}{\partial x}\Big|_{x=0} u(x,t) = \kappa \frac{\partial}{\partial x}\Big|_{x=0} \int_r^R dy \int_0^{\infty} ds\, cos(\omega\, s) \int_{-\infty}^{\infty} \frac{d\varpi}{2\pi} \int_{-\infty}^{\infty} \frac{dk}{2\pi} \frac{e^{ikx+i\varpi(t-s)}}{\lambda^2 k^2 + \alpha(\varpi) + i\beta(\varpi)} \left(e^{-iky} - e^{iky}\right) =$$

$$= \kappa[F(r,t;\omega) - F(R,t;\omega)]$$

Where

$$F(r,t;\omega) = \frac{exp(-p(\omega)r/\lambda)}{\lambda\sqrt{p(\omega)^2+q(\omega)^2}} cos(\omega\, t - q(\omega)\frac{r}{\lambda} - arctan(\frac{q(\omega)}{p(\omega)}))$$

with

$$p(\omega) = \sqrt{\frac{\sqrt{\alpha(\omega)^2+\beta(\omega)^2}+\alpha(\omega)}{2}} \text{ and } q(\omega) = \sqrt{\frac{\sqrt{\alpha(\omega)^2+\beta(\omega)^2}-\alpha(\omega)}{2}}$$

This means that illuminating a band of the cable with a sinusoidal temporal envelope generates a somatic current injection with two sinusoidal contributions, each with an amplitude that decays exponentially with distance of the boundaries of the band from the soma and each with two contributions to the phase shift relative to the phase of the input. One shift that scales with the distance and another that does not. The spatial decay and all phase shifts increase with the driving frequency *f*.

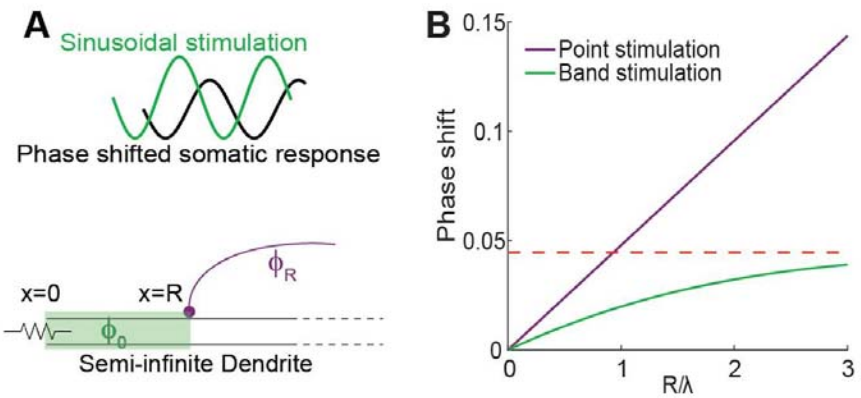

Figure 1: A cable theoretic model of optogenetic dendritic activation. A: Our model of the dendrite consists of a semi-infinite linear cable, where the somatic boundary at *x=0* is kept at a constant holding potential $u(0,t)=u_0$. Optogenetic stimulation is modeled as a band of illumination starting at the soma and ending at *R* (green). Alternatively, *x=R* can be the locus of a point illumination (purple). Stimulus is a temporal sine waveform (green) and the somatic current response is an attenuated and phase shifted version of it (black). **B:** The phase shift between a sinusoidal optogenetic stimulation and the corresponding somatic current response as a function of the ratio between *R* and the dendrite's electrotonic distance λ for band (green) and point stimulation (purple). The phase shift for band stimulation is bounded (red), while point stimulation is not bounded. Both curves are calculated for *f=10 Hz* and τ = 10 *ms*.

To measure the resulting phase shift between the injected current $cos(\omega\, t)$ and the somatic current response *I(t)*, we calculate the location of the peak of the cross-correlation function (CCF) between them by averaging their product over all time. The CCF is given by:

$$C(\Delta) = \langle cos(\omega\,[t-\Delta])I(t)\rangle = \kappa[F(r,\Delta;\omega) - F(R,\Delta;\omega)]/2$$

Differentiating with respect to Δ and comparing to zero results in the following equation:

$$sin(\omega\,\Delta - q(\omega)\tfrac{R}{\lambda} - arctan(\tfrac{q(\omega)}{p(\omega)}) + q(\omega)\tfrac{\delta R}{\lambda}) = e^{-p(\omega)\frac{\delta R}{\lambda}} sin(\omega\,\Delta - q(\omega)\tfrac{R}{\lambda} - arctan(\tfrac{q(\omega)}{p(\omega)})$$

where $\delta R \overset{\text{def}}{=} R - r > 0$. This equation can be used to find the phase shift $\Phi = \omega\,\Delta$ corresponding to the peak in the CCF. We consider two cases:

Case I - the stimulated region is small compared to the electrotonic length ($\delta R \ll \lambda$):

In this case, after linearization we get the equation

$$\Phi_R = \omega\,\Delta = \tfrac{R}{\lambda} q(\omega)\ mod\ 2\pi \quad [1]$$

At this limit, the phase behaves like the stimulation of a single point at distance *R* from the soma (Fig. 1A, purple dot).

Case II - the stimulated region begins at the soma ($r = 0$):

In this case (Fig. 1A, green band), we get

$$\Phi_0 = \omega\,\Delta = arctan(\tfrac{q(\omega)}{p(\omega)}) - arctan\ \frac{sin\ \frac{R}{\lambda} q(\omega)}{e^{\frac{R}{\lambda} p(\omega)} - cos\ \frac{R}{\lambda} q(\omega)} \quad [2]$$

To summarize, the model allows us to calculate the current injected by the cable into the soma in response to a sinusoidal current perturbation with frequency *f*, given at some location *R* in the dendrite (case I), or applied to a region of the dendrite (case II). Our analysis shows that the current arriving at the soma is also sinusoidal, but it lags by a phase delay of $\Phi_R/2\pi$ or $\Phi_0/2\pi$, respectively.

Note that the phase delay following a field stimulation is bounded in the case of a linear dendrite [*e.g.*, $\alpha(\omega) = 1$ and $\beta(\omega) = \omega\tau$], as the distance from the soma grows ($\frac{R}{\lambda} \to \infty$, eq. 2). In contrast, the phase shift in response to point stimulation (eq. 1), continues to increase linearly with the distance from the soma (Fig. 1B).

Investigating the electrotonic structure of SNr dendrites

To measure the effect of the dendritic localization of inputs on the somatic current response, we used transgenic mice that express ChR2 throughout the entire somatodendritic arbor of SNr neurons (42,43). We chose to compare two extreme cases: illuminating either the soma alone (including perhaps very proximal dendrites) or the entire dendritic tree. This choice was motivated by three considerations. First, we reasoned that the strategy of illuminating the entire region is likely to create a more consistent and robust effect across diverse geometries of dendritic arbors. Similarly, illumination restricted to the somata is also more readily comparable between cells. Second, the cable theoretic model we use to fit the data is more applicable under these conditions, as illuminating a band of cable in the model is comparable to illuminating an annulus in the plane, centered around the soma. Finally, both situations could conceivably be physiologically relevant. Coherent rhythmic input could arise under physiological conditions such as sleep (16,44) and pathophysiological conditions, such as parkinsonism (18,45). Coherent pallidal input would preferentially target the soma (38,39,41), whereas coherent subthalamic or striatal input could activate the entire dendritic arbor (36,37). Hence, we optogenetically stimulated the ChR2-laden SNr neurons using 470 nm LED light that was sinusoidally modulated at various temporal frequencies (0.25 to 16 Hz, 3-4 seconds of stimulation per frequency), while blocking all glutamatergic and GABAergic inputs. The cell was held at –70 mV to prevent spiking, and the current injected to the soma was measured in whole-cell voltage clamp. This was repeated under two stimulation conditions: a) proximal

stimulation targeting the soma and proximal dendrites; and b) full-field illumination exciting the soma as well as the entire dendritic arbor (Fig. 2A).

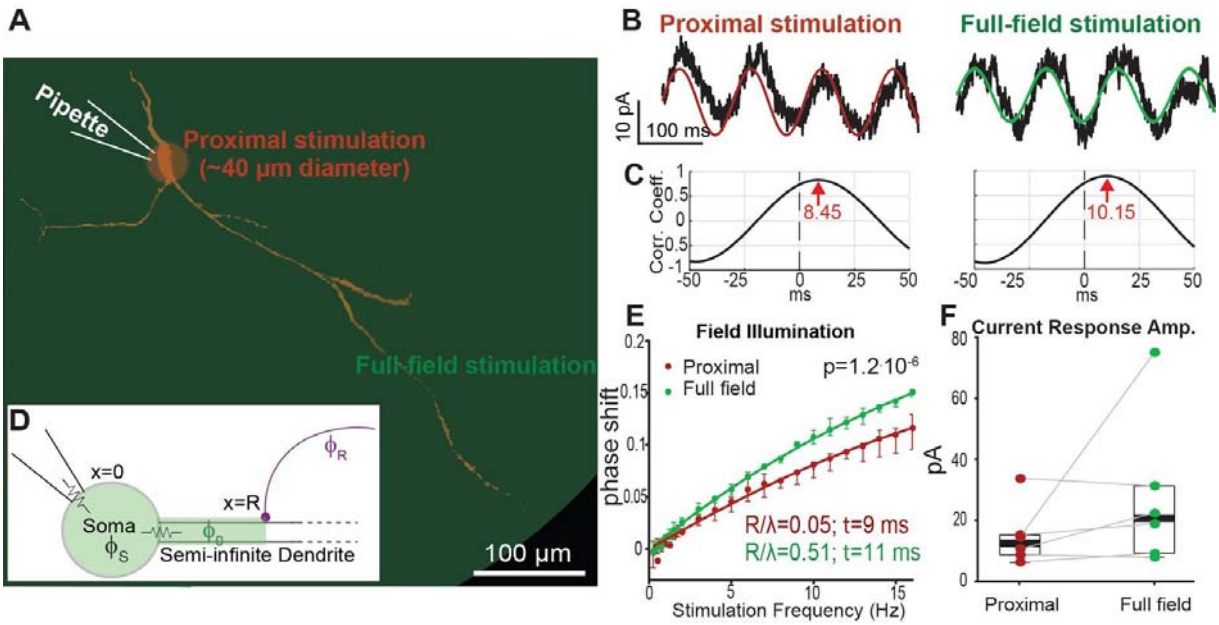

Figure 2: Somatic current responses to periodic illuminations of SNr GABAergic neurons shift depending on the size of the dendritic arbor activated. A: Collapsed two-photon image of typical SNr GABAergic neuron, filled with Alexa Flour. To compare distal and proximal inputs, optogenetic stimulation was applied under two conditions: 1) illuminating a diameter of ~40 mm around the soma, targeting the soma and proximal dendrites (proximal, red); and 2) full-field illumination stimulating the entire dendritic arbor (full-field illustration). **B:** Optogenetic sinusoidal waveforms at various frequencies (0.25-16 Hz) were delivered under the proximal (red) and full-field (green) stimulation conditions. Somatic whole-cell current response (black) is a phase shifted sinusoid. **C:** Phase shift between optogenetic periodic stimulation and somatic current response was determined by the location of the peak in the cross-correlation function between the two traces (red arrows). **D:** The model used to fit the data consists of a semi-infinite cable, as in figure 2A, that is connected to an isopotential soma which adds an additional angular phase Φ_S . **E:** Proximal and full-field illumination conditions give rise to two distinct curves (n=6; $p=1.2\cdot10^{-6}$, ANCOVA). The response to rhythmic stimulation shows a clear spatial effect – phase shift between stimulation and somatic response is larger under full-field illumination (green) compared to proximal (red). Under the assumption of a linear dendrite, we attain a good agreement between the predictions of our model ($(\Phi_0 + \Phi_S)/2\pi$, lines) and empirical results (points). Error bars represent standard error of the mean. **F:** Amplitude of somatic current response was comparable between the proximal and full-field stimulation conditions. Central marks indicate the median and box edges represent 25th and 75th percentiles

The current measured with a patch electrode at the soma in response to the sinusoidal optogenetic stimulation was a phase shifted sinusoidal waveform of the same temporal frequency (Fig. 2B). The phase shift between the periodic stimulation and the somatic response was determined by the location of the peak in the CCF between the two traces (Fig. 2C). This was used to generate a plot of the phase shift as a function of stimulation frequency for each illumination condition (Fig. 2E). Amplitudes of somatic current responses were similar for proximal and full-field illumination (Fig. 2F), but the two spatial conditions give rise to distinct curves (n=6; $p = 1.2 \cdot 10^{-6}$, ANCOVA). As expected, the phase increases with frequency in both conditions. However, the phase shift between the stimulation and the somatic current response is larger when the entire dendritic field is illuminated compared to only the soma and proximal dendrites (Fig. 2E). Thus, the response of SNr GABAergic neurons to subthreshold rhythmic stimulation shows a clear spatial effect, indicating that optogenetic methods can reveal the electrotonic structure of the dendrites and their contribution to somatic currents. Importantly, the experiment was repeated with holding voltages of –60 mV and –50 mV and yielded the same results, indicating that there is no voltage dependence of the phase shifts in the subthreshold range. In other words, the dendrites do not exhibit substantial subthreshold nonlinearities.

In order to estimate the electrotonic properties of SNr dendrites, we fit our data to the cable theoretic model (46). The empirical curves describing the dependence of the phase shift on frequency were fit to the appropriate case II of the model (eq. 2). Because the electrode does not measure the current injected by the dendrite into soma directly, but rather the current at the patch pipette tip, we need to add to the dendritic phase shift (predicted by the model) the phase introduced by the somatic membrane (Fig. 2D). Assuming an isopotential passive membrane (which is a good approximation when holding at subthreshold voltages) yields the additional angular phase of $\Phi_S = arctan\,(2\pi f \tau)$ (Fig. 2D). Even with the simplifying assumption of a strictly passive linear dendrite – which is certainly in line with the voltage independence of the phase shift we described above – we attain a good agreement between the predictions of our model and the empirically observed average frequency dependent phase shift at the

soma (Fig. 2E). Fitting our theoretical curve to the empirical data for the two conditions results in similar and physiologically plausible (47) values for the membrane time constants (i.e., $\tau_{proximal} = 9ms$, $\tau_{full-field} = 11ms$) and the space constant λ. The ratio of the boundary of the stimulated region to the dendritic space constant ($\rho = \frac{R}{\lambda}$) was also extracted ($\rho_{proximal} = 0.05$, $\rho_{full-field} = 0.51$). From $\rho_{proximal}$ we can deduce that the effective space constant of the SNr dendrites is approximately 400 µm (=20 µm/0.05) (47). Moreover, the model estimates that the value corresponding to illumination of the entire dendritic field is ~10 times larger than the value for illumination of only the soma and proximal dendrites. Therefore, we can deduce that on average dendrites are light-activated out to 200 µm from the soma. This is a reasonable estimate, considering that in acute slices regions beyond that are often cut or are too deep to be affected by the illumination. In summary, our theoretical and experimental results demonstrate that distal and proximal inputs undergo different phase shifts by the time they reach the soma. We therefore hypothesize that these different phase shifts will also differentially affect the suprathreshold behavior of these pacemaking neurons.

Proximal and full-field PRC estimation

To address this hypothesis, we estimated proximal and full-field PRCs by incorporating our two illumination conditions into a previously described method for PRC measurement using optogenetic pulses (43). The neurons were subjected to Poisson-like processes composed of barrages 0.5-1 ms long light pulses, separated by exponentially distributed inter-pulse intervals (Fig. 3A, see Methods).

In order to examine the ChR2 currents generated by the barrage stimulation, cells were hyperpolarized to prevent spiking and steady-state currents (4-9 seconds after beginning of stimulation to avoid any effects of ChR2 deactivation) were measured in the whole-cell voltage clamp configuration (Fig. 3A). For each cell (n=11), a curve portraying the average current response to a light pulse was generated (Fig. 3B). As previously reported, average responses were well fit by a double exponential, chosen to accommodate

ChR2 deactivation kinetics (43) (eq. 9, see Materials and Methods), and rise and decay time constants (τ_{rise}, τ_{decay}) were extracted. Rise time constants were significantly larger when the entire dendritic tree was illuminated compared to only the soma and proximal dendrites. This is evident in the distribution of rise time constants ($p = 8.15 \cdot 10^{-5}$, RST) (Fig. 3C), as well as the average current response curves for the different conditions (Fig. 3B). The delayed peak of the somatic response when the entire dendritic tree is illuminated is consistent with the delayed full-field response that we observed in the previous section. Thus, the barrage stimulation induces disparate somatic current profiles under the proximal and full-field stimulation conditions.

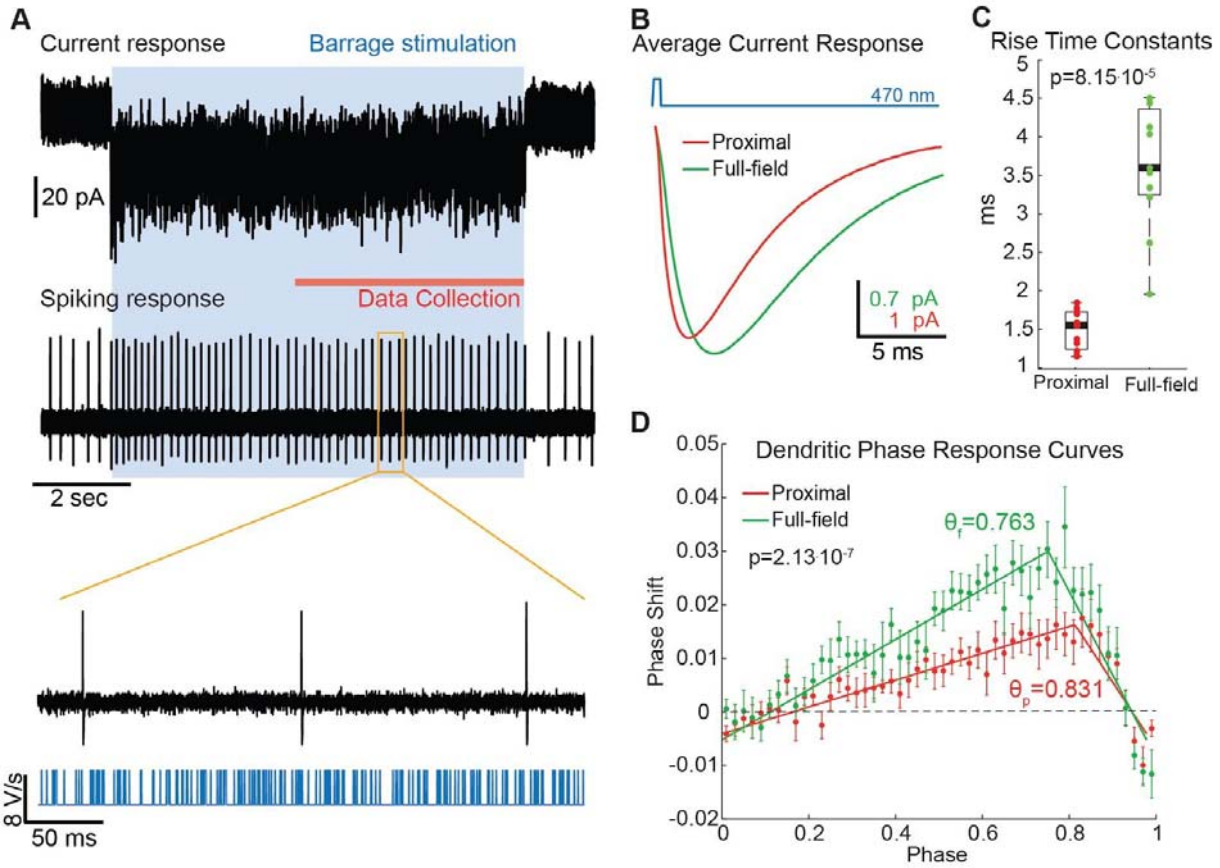

Figure 3: Proximal and full-field barrage stimulations generate distinct PRCs in SNr GABAergic pacemakers. A: ChR2 current and spiking responses (top, black) to barrage stimulation (bottom, blue). The stimulus generated an inward current in whole-cell voltage clamp and an increase in firing rate in cell-attached current clamp. Blue shading indicates stimulation time and red line marks the period in which ChR2 responses have reached steady-state and data is collected. **B:** ChR2 current responses to a light pulse (blue), averaged over all pulses and all cells (n=11). Full-field illumination (green)

induces a wider response than proximal illumination (red). **C:** For each stimulation condition, a double exponential was fit to the average current responses for each cell and time constants were extracted ($\tau_{rise}, \tau_{decay}$). The distribution of rise time constants is significantly different in the two stimulation conditions ($p=8.15 \cdot 10^{-5}$, RST), and values are larger in the full-field condition compared to proximal. Central marks indicate the median and box edges represent 25th and 75th percentiles. **D:** Barrage stimulation was used to measure PRCs corresponding to the two stimulation conditions. Points are the empirical data and lines represent the fitted curves. Proximal and full-field illumination resulted in two distinct PRCs (n=19, $p=2.13 \cdot 10^{-7}$, ANCOVA), with the peak of the full-field curve occuring at an earlier phase than that of the proximal one (θ_f=0.763 and θ_p=0.831, respectively). Error bars represent standard error of the mean.

We have shown previously that the more distal a dendritic perturbation is, the more leftward a shift it will generate in the dendritic PRC compared to the somatic one (32). Thus, the shift we observed in the current profile generated by the full-field illumination relative to the proximal one buttresses the hypothesis that the empirical PRC measured under the full-field illumination should exhibit a leftward shift relative to that measured under proximal illumination. To test this hypothesis, we applied the barrage stimulation to spontaneously firing SNr cells recorded in the cell attached configuration (Fig. 3A) and estimated the two PRCs corresponding to the proximal and full-field illumination conditions. For each stimulation condition and for every cell, the PRC was estimated using a multiple linear regression method (43,48) (see Materials and Methods). Previous measurements of the PRCs of SNr GABAergic pacemakers reveal a triangular form - the PRC slopes upwards before peaking and falling to zero as the phase approaches 1 (43). We therefore fit a triangle (parameterized by a single location parameter $0 < \theta < 1$ of the peak) to our experimental data (see Materials and Methods), in order to extract the location of the peak.

Our analysis results in two distinct average PRCs (n=19; $p = 2.13 \cdot 10^{-7}$, ANCOVA), with the full-field PRC peaking before the proximal one (Fig. 3D). The steep negative slope at late phases represents the cells approaching the causal limit, where the input elicits an immediate spike (49). According to our theoretical model, as well as the results of our study of the dendrite's electrotonic structure, the somatic current generated by a stimulation delivered in the full-field condition would be phase delayed compared

to a proximal stimulation, which explains why the peak of the full-field PRC is shifted leftward relative to the proximal PRC.

Hence, differentially located inputs arrive at the soma at different times, thereby shifting the full-field PRC leftward relative to the proximal one. Next, we turn to measure properties of the collective activity of SNr pacemakers which theory predicts are dependent on the shape of the PRC (49–51). First, we measure the fidelity and latency of the population response of SNr neurons to sudden changes in their input, and we then consider the propensity of rhythmic inputs to entrain SNr pacemaker neurons.

Populations response to proximal vs. full-field stimulation

Barrage stimulation changed the firing frequency of SNr GABAergic cells (Fig. 4A). The perturbation significantly increased the pacemaker's mean firing rate by 33% for proximal (n=19; $p = 7.7 \cdot 10^{-8}$, SRT) and by 19% for full-field (n=19; $p = 7.7 \cdot 10^{-8}$, SRT) illumination (Fig. 4B). In a population of cells, the response to a step stimulation consists of two stages - an initial increase in firing and a relaxation to a steady-state rate. The rapidity at which the PSTH can track the change in inputs is a measure of the fidelity of the neurons' coding of the input. The Fokker-Planck formalism enables one to predict how the PSTH is related to the PRC (See eq. 8 in Materials and Methods) (50,51). Interestingly, this connection demonstrates that the initial rise in the PSTH should reflect the mirror image of the falling phase of the PRC (50). Thus, the leftward shift in the full-field PRC should generate a rightward shift in the rise time of the the full-field PSTH relative to the proximal PSTH. Estimation of the empirical PSTHs under both conditions confirmed this prediction, with the peak in the proximal PSTH appearing approximately 12 ms before that of the full-field PSTH (Fig. 4C). Moreover, fitting the empirical PSTH to the theoretical equation for the PSTH with an underlying triangular PRC, enables us to extract independent estimates of the peak of the triangular PRC based on the rise time of the PSTH $(\theta_p = 0.901,\ \theta_f = 0.733)$. Indeed, this estimation gave rise to a larger (but comparable) estimate of the

phase shift between the peaks of the underlying proximal and full-field PRCs. A caveat in PRC estimation is the difficulty to estimate it empirically near the causal limit (49). Thus, for weak perturbations, values of PRC peaks extracted from the PSTHs may provide a more precise estimation of the true shape of PRC's late downswing, which may be occluded by the causal limit.

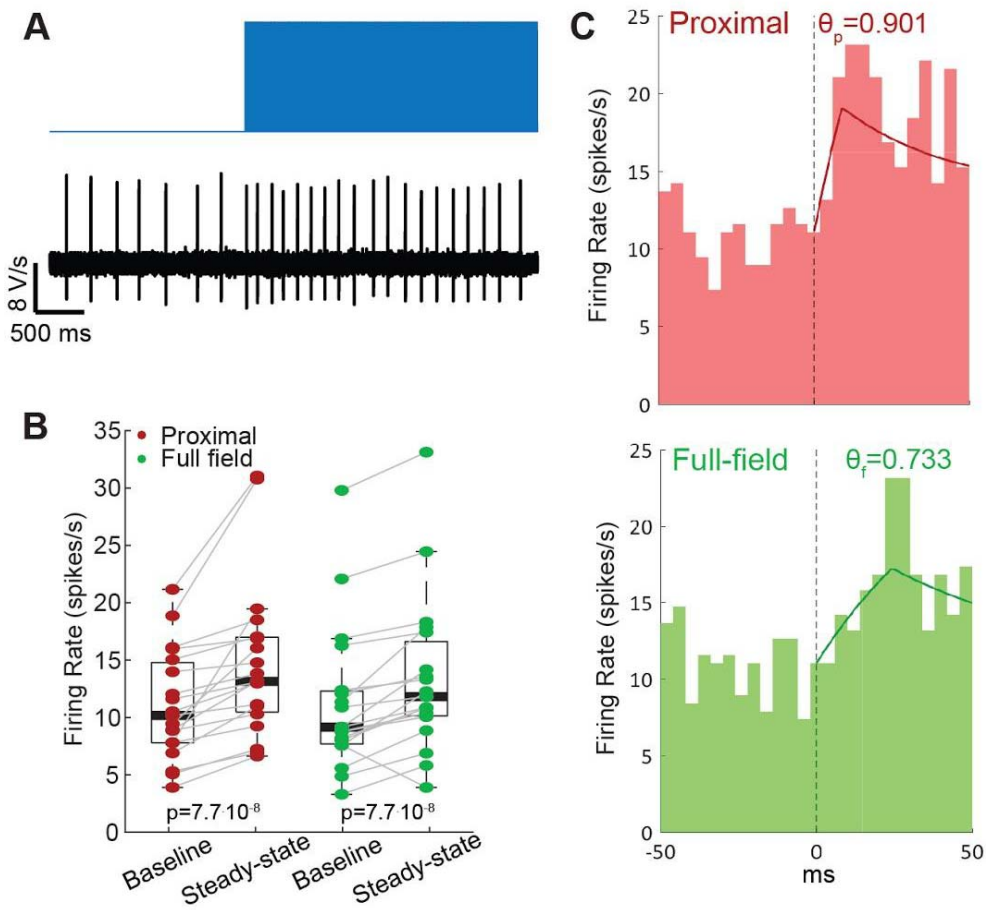

Figure 4: Proximal and full-field barrage stimulations induce distinct peri-stimulus time histograms (PSTHs). A: Example of an increase in the cell's firing rate in response to barrage stimulation. **B:** Baseline and steady-state firing rates were similar under the proximal (red) and full-field (green) stimulation conditions (n=19). Barrage stimulation increased the firing rate significantly ($p = 7.7 \cdot 10^{-8}$, SRT). Central marks indicate the median firing rates and box edges represent 25th and 75th percentiles **C:** Peristimulus time histograms (n=19 cells, 25 repetitions per cell) centered around stimulus onset. The peak in population firing rate response to stimulus onset is delayed by approximately 12 ms in the full-field illumination condition (green) compared to the proximal illumination condition (red). Lines represent fitted theoretical curves, corresponding to θ_f=0.733 and θ_p=0.901.

Entrainment of SNr pacemakers to rhythmic inputs

The discharge of a regularly active neuron can be entrained by small amplitude sinusoidal currents delivered to the soma, when the driving frequency is close to the neuron's natural firing rate (or to integer multiples of it). Within this range of frequencies, the rhythmic stimulation reshapes the neuron's firing pattern - the firing rate changes to match that of the periodic stimulation and becomes phase locked to it (52). SNr neurons were allowed to fire spontaneously and their spiking activity was recorded in the perforated patch current clamp configuration. The perforated patch configuration was chosen to allow us to see subthreshold responses and injected somatic currents, while avoiding the disruption of pacemaking activity by the disruption of the neurons intracellular milieu.

A 30-60 seconds long 10-20 pA cosine shaped current of frequency f was injected into the soma of spontaneously firing cells (example in Fig. 5A). We studied the effect of the oscillatory input on the cell's firing pattern based on a previously published method (52). For each spike, we measured the duration of the next perturbed period, denoted T_p, of the neuron's spiking as a function of its effective phase, the phase ψ in the period of the sinusoidal input in which the spike occurred, and fit a periodic function comprised of 3 modes to the effective mode, resulting in the function $T_p(\psi)$ (Fig. 5B). Given an initial action potential at the effective phase ψ_n, we can predict the effective phase ψ_{n+1} of the next action potential using the following iterative mapping:

$$\psi_{n+1} = (\psi_n + \frac{T_p(\psi_n)}{T})\ mod\ 1 \quad [3]$$

Therefore, the evolution of the phase of spiking relative to the oscillatory input can be represented using an iterative map. An intersection between the map and the diagonal (where $\psi_{n+1} = \psi_n$) represents a fixed point of the dynamics. When the slope of the iterative map at the fixed point is smaller than unity, the fixed point is stable and the neuron is phase-locked with the stimulus. Thus, the sequence of phases visited by the neuron over a series of spikes can be predicted via this iterative map (52,53).

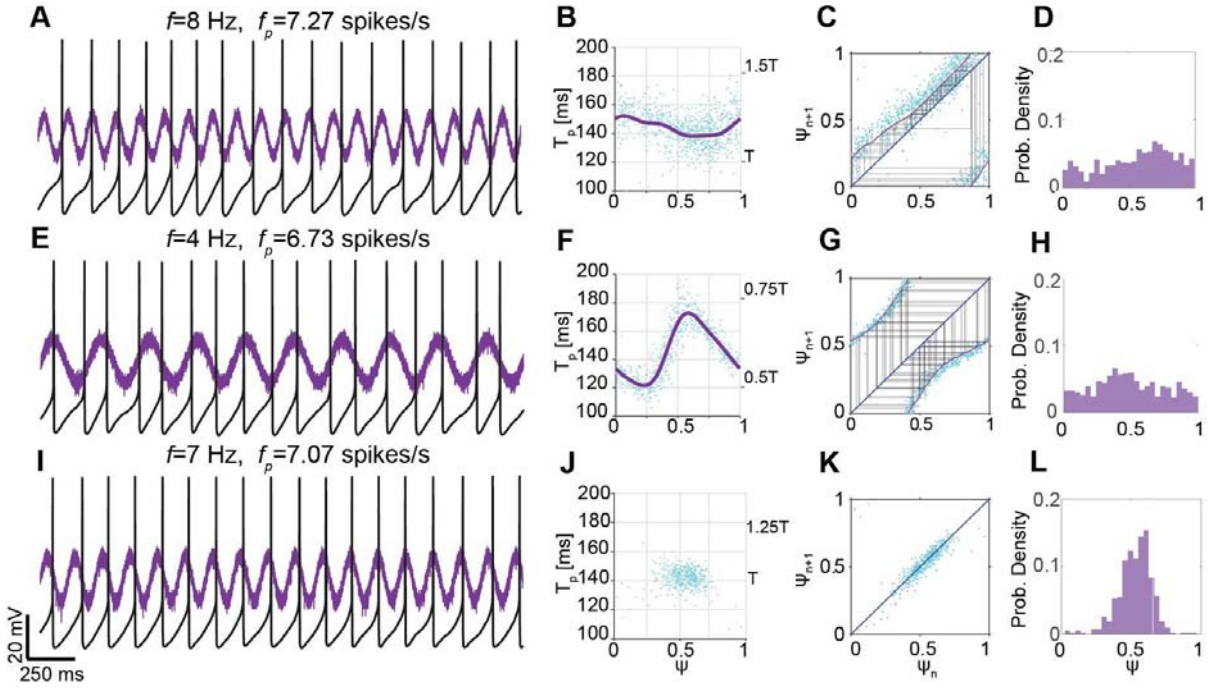

Figure 5: Entrainment of the spiking of SNr GABAergic pacemakers using sinusoidal somatic current injection. A: Perforated patch recording of a spontaneously firing cell with an average perturbed firing rate f_p, as a cosine shaped current of frequency f was injected into the soma. When f is sufficiently larger than the natural firing rate f_0, the pacemaker's firing is not phase-locked to the periodic input. **B:** Scatter plot of the perturbed period of the cell's spiking T_p as a function of the effective phase ψ in which the spike occurred (cyan). Fitted curve (purple) was used to generate the iterative mapping shown in C. Right-hand-side y-scale shows T_p in units of T, the period of the rhythmic stimulus. **C:** An iterative map of the effective phase of the next spike ψ_{n+1} versus that of the current spike ψ_n (purple). Dots represent empirical data, and the mapping is generated from the fitted curve in B. The map is mostly above the diagonal and does not transect it (blue). Cobweb plot (black) uncovers chaotic dynamics. **D:** The distribution of effective phases is broad and samples the entire range between 0 and 1. **E, F:** Same as A, B with $f<f_0$. **G:** Same as C with $f<f_0$. The map (purple) is mostly below the diagonal (blue) and does not transect it. **H:** Same as D with $f<f_0$. **I:** When $f\sim f_0$, the cell's spiking is phase-locked to the oscillatory input. The spike tends to occur at or slightly after the peak of the stimulus. **J:** Due to phase locking, the cell visits a narrow range of effective phases. All points of the perturbed period versus the effective phase are gathered around the equivalent phases 0 and 1. The period of the cell's spiking is approximately constant and equal to the period of the stimulus T. **K:** Mapping cannot be evaluated. All phase points are located on the diagonal and around phases 0 and 1, indicating phase locking. **L:** The distribution of effective phases shows a clear peak around the phase of entrainment (~0.6).

The fitted curve for the measurements of T_p as a function of ψ (Fig. 5B) was used to generate an iterative map of effective phases (eq. 3). Note that the mapping closely traces the empirical scatter plot of ψ_{n+1} versus ψ_n (Fig. 5C). In the example presented in figure 5, the cell was spiking spontaneously at a frequency $f_0 \approx 7$ spikes/s throughout the recording. When the stimulation frequency f is larger than the cell's natural firing frequency f_0 (Fig. 5C), the map passes mostly above the diagonal and does not transect it, which is consistent with the lack of phase locking in the raw data (Fig 5A). The lack of phase locking is evident in the chaotic dynamics exhibited by the iterative mapping of effective phases (Fig. 5C), as well as in the wide probability distribution of effective phases covering all phases between 0 and 1 (Fig. 5D). When $f < f_0$ (Fig. 5E), the map passes below the diagonal. Again, the neuron's firing is not entrained by the periodic stimulation and the effective phase mapping gives rise to chaotic dynamics (Fig. 5G). Nevertheless, the distribution of phases in both cases (Fig. 5D,H) show an accumulation of phases in the area where the map passes closest to the diagonal (Fig. 5C,G), demonstrating the effect of the sinusoidal input.

When $f \sim f_0$, the firing of the cell is phase-locked to the stimulus at a phase close to 0.5 (Fig. 5I). In this case, the pacemaker only visits a limited range of effective phases. Therefore, we cannot fit a curve to T_p measurements (Fig. 5J) and an iterative map (eq. 3) cannot be evaluated. Nevertheless, the entrainment of the neuron's firing to the periodic input is clear from the narrow distribution of points in the scatter plot of ψ_{n+1} versus ψ_n and their accumulation on the diagonal (Fig. 5K), as well as the sharp peaks around the equivalent phases 0 and 1 in the probability distribution of effective phases (Fig. 5L).

Next, we incorporate optogenetic excitation into this scheme. The experiment above was repeated, but the temporal cosine waveform stimulation was applied optogenetically using the two spatial conditions of proximal (Fig. 6A) and full-field (Fig. 6E) illumination. Depending on the ratio between the stimulation frequency f and the natural firing frequency of the cell f_0, the stimulus either entrained the spiking activity of the cell, or was ineffective in causing entrainment. The efficacy in phase locking also differed somewhat between the two conditions, with full-field illumination inducing entrainment more readily. In

order to examine the dendritic effect on entrainment, we focused on instances where phase locking was obtained.

To obtain a deeper understanding of the effect of the portion of the dendritic arbor being activated on entrainment, we performed a simulation. When phase locking occurs, the pacemaker samples a narrow range of effective phases around the phase of entrainment, and it is thus impossible to estimate an *empirical* curve relating the perturbed period to the effective phase. However, the perturbed period can be described using the following *theoretical* equation

$$T_p(\psi) = T_0(1 - \Delta\varphi(\psi)) \quad [4]$$

Where T_0 is the unperturbed period of the oscillating neuron, and $\Delta\varphi$ is the change in the intrinsic phase of the neuron induced by the stimulus. The evolution of intrinsic phase in response to a cosine shaped stimulation depends on the pacemaker's PRC, denoted by *Z*, and is given by

$$\frac{d\varphi}{dt} = f_0 - A\cos(2\pi[ft + \psi])Z(\varphi) \quad [5]$$

We evaluated the change in intrinsic phase $\Delta\varphi$ by numerically integrating eq. 5 until the intrinsic phase φ reaches 1 and measuring the resulting change $\Delta\varphi$ for various values of the effective phase ψ. PRCs were modeled as triangles peaking at $\theta_p = 0.9$ and $\theta_f = 0.75$ (values similar to those extracted from PSTH estimates) for proximal and full-field illumination, respectively. Both f and f_0 were set to 7 Hz $(A = 5)$. Simulated $\Delta\varphi$ values were plugged into eq. 4, generating a *numerical* curve of T_p as a function of ψ predicted by the phase dynamics and the PRC (Fig. 6B,F). This curve was then used to evaluate a mapping for the evolution of effective phases (eq. 3) under each illumination condition (Fig. 6C,G).

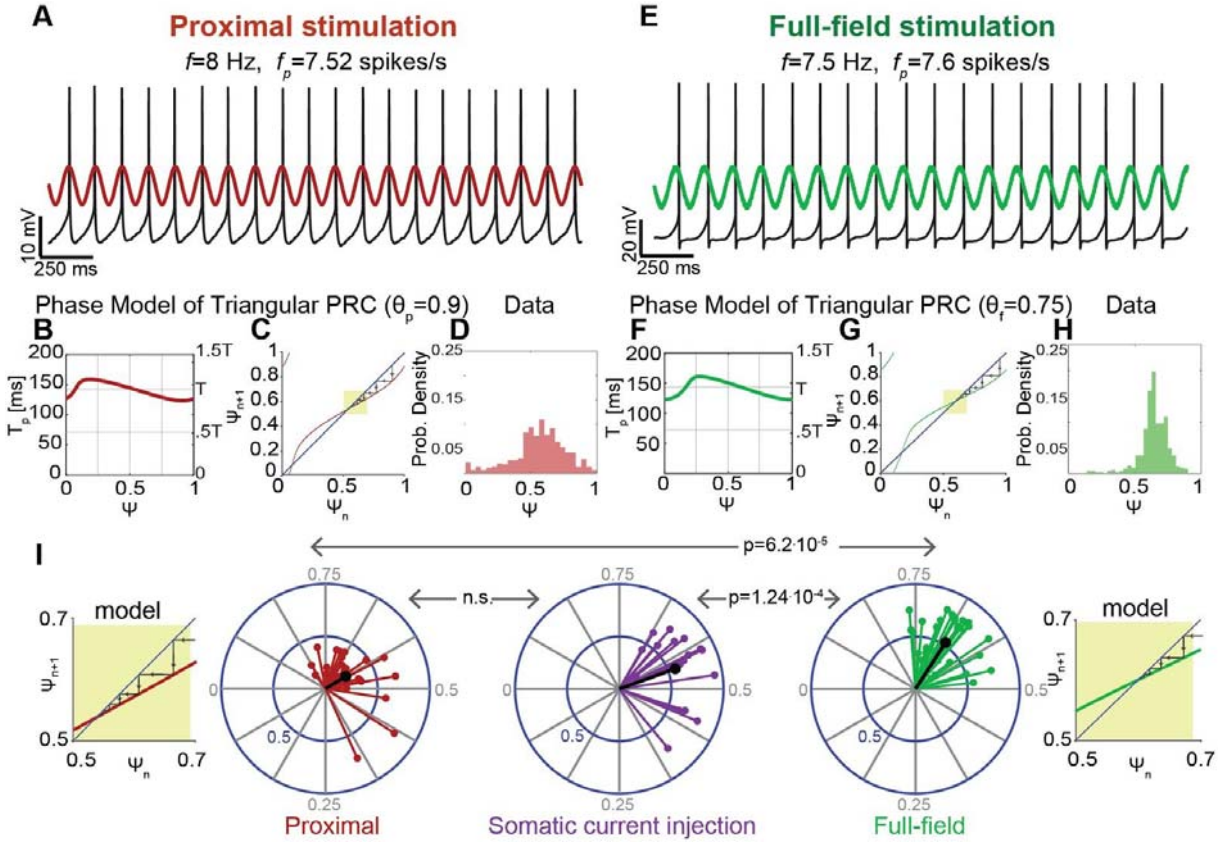

Figure 6: The dendrite impacts the phase of entrainment to rhythmic inputs. A: Perforated patch recording of a spontaneously spiking neuron with an average perturbed firing rate f_p. A cosine shaped stimulation delivered in the proximal illumination condition entrained the discharge of the cell. The spike tends to occur near the peak of the stimulation, corresponding to phases near 0.5. **B:** Simulated (eq. 5) plot of the perturbed period (T_p) as a function of the effective phase of the preceding spike (for $\theta_p = 0.9$). **C:** Mapping of ψ_{n+1} versus ψ_n generated based on the simulated plot shown in B. The mapping (red) crosses the diagonal (blue), achieving a stable fixed point at phase 0.537, as demonstrated by the Cobweb plot (black arrows). Yellow box highlights stable fixed point. **D:** The probability distribution of effective phases shows a peak at early phases, in accordance with the raw data shown in A. **E:** Same as A for full-field illumination. Spikes occur slightly after peak of cosine stimulation. **F:** Same as B for full-field illumination (for $\theta_f = 0.75$). **G:** Same as C for full-field illumination. The mapping (green) crosses the diagonal (blue), generating a stable fixed point at phase 0.6. Phase locking induced by full-field stimulation occurs at a delayed phase compared to proximal stimulation (shown in A-D). **H:** Same as D for full-field illumination. The phase of the peak in the probability distribution is later than that corresponding to proximal illumination and shown in D. **I:** Distribution of circular variances of effective phases (each calculated from a corresponding probability distribution of effective phase as in panels D and H) for various stimulation frequencies (2.5-21Hz) in n=6 cells, under three stimulation conditions: proximal illumination (red), somatic current injection (purple) and full-field illumination

(green). Mean vectors are shown in black. Proximal illumination and somatic current injection induce locking in a similar range of phases, but current injection is more effective in entraining the neuron's spiking. Phase locking generated by full-field illumination is shifted rightward compared to proximal illumination and current injection by 0.572-0.604. Yellow insets are zoomed-in versions of panels C and G that show that the shift in the model of the empirical distribution of locked phases agrees with the phase model simulations. P-values derived using the RST.

Both simulated mappings intersect with the diagonal achieving stable fixed points, which represent the effective phases of locking between the neuron's spiking activity and the oscillatory stimulation. When a large portion of the dendritic field is stimulated, phase locking is predicted by the phase dynamics to occur at the phase 0.6 (Fig. 6G). In contrast, the predicted phase of locking corresponding to proximal stimulation is 0.537 (Fig. 6C). Thus, our simulation predicts that the effective phase of entrainment will occur slightly after the peak of the driving sinusoid and that this locking phase will be delayed when the entire dendritic arbor is stimulated compared to when only the soma and proximal dendrites are stimulated. This is consistent with the relative locations of the peaks in the probability distributions of empirical effective phases under the two spatial conditions (Fig. 6D,H).

This experiment was repeated using various stimulation frequencies (2.5-21Hz) in several cells (n=6). Oscillatory stimulation was delivered either optogenetically using proximal or full-field illumination, or as somatic current injection. For each trial, a probability distribution of effective phases was generated (Figs. 6D,H), and was used to calculate a circular variance vector (54) (see Materials and Methods). The argument of this complex vector represents the phase of locking between firing activity and the periodic stimulus, and its amplitude expresses the strength of locking. Because we are interested in instances of entrainment, only trials with circular variance amplitudes above a threshold determined by bootstrapping were included in the analysis (see Materials and Methods). While somatic current injection was more effective at inducing entrainment than proximal illumination (Fig. 6I), both stimulation conditions generated similar ranges of locking phases (averaging at 0.555 and 0.587 for current injection and proximal illumination, respectively). This suggests that the proximal stimulation condition, in which only the soma and proximal dendrites are activated optogenetically, is comparable to somatic current

injections. In contrast, the typical phase of locking in the full-field illumination condition (averaging at 0.6585) is significantly delayed compared to the proximal illumination ($p = 6.2 \cdot 10^{-5}$, RST) or somatic current injections ($p = 1.24 \cdot 10^{-4}$, RST). Thus, the effective phase of the entrainment (shortly after the peak of the stimulation) and the difference between locking phases corresponds to those predicted by our simulation (Fig. 6C.G), which was based on the empirical PRCs for the two illumination conditions (Fig. 3D). The divergence of the PRCs, in turn, is explained by the electrotonic properties of the dendrites of the SNr GABA neurons (Figs. 2 & 3).

Discussion

Predictive models of dendritic neurons

To capture the entire dynamical repertoire of a neuron requires a detailed and high-dimensional model (55–57). However, pacemaker neurons (and their corresponding models) offer an opportunity for simplification. Pacemakers traverse a low-dimensional closed contour called a limit cycle, so the high-dimensionality of the individual neuron can usually be shed in favor of a simpler dynamical system that captures the essence of the limit-cycle. The phase reduction method is a powerful formalism that does precisely that (19–22,58,59). It reduces the pacemaker to a phase oscillator represented by its intrinsic frequency and its PRC, while maintaining the robustness and universality of pacemakers and oscillators. Pacemakers are attractive because the core of their dynamical properties *can* be measured and quantified in a single experiment. Many studies have capitalized on this and successfully measured empirical PRCs in order to characterize neuronal pacemakers and their collective dynamics (22–24,27,29,30).

However, reducing pacemakers to a phase oscillator with a single PRC, overlooks the contribution of their morphology to the phase dynamics. In the current study, we worked within the formalism of phase reduction theory, but still preserved the essential contribution of the dendritic arbor to the pacemaker's

502 dynamics. We combined results from cable theory, phase reduction theory, statistical physics and
503 nonlinear dynamical theory to elaborate how the spatial extent of dendritic activation dictates the
504 structure of the PRC and how that in turn characterizes how dendrites affect the population rate response
505 and entrainment of pacemaker neurons. Remarkably, the very simple cable model in combination with
506 these powerful and generic theories, gave rise to predictions that were then corroborated experimentally,
507 without needing to invoke detailed morphologies or ionic currents.

508 *Interrogating electrotonic structure of SNr neurons with sinusoidal optogenetic inputs*

509 We began our combined theoretical and experimental study by investigating the electrotonic structure of
510 SNr GABAergic pacemakers, and generating a model that accurately predicts the somatic response to
511 input arising from different synaptic locations in the dendritic tree. Although our formalism can detect
512 dendritic nonlinearities, our analysis showed that SNr GABAergic pacemakers and their dendrites are
513 mostly linear. This is supported by the good fit we obtained between the empirical data and the model
514 under the assumption of a linear dendrite (Fig. 2E), as well as the fact that the effect was not dependent
515 upon holding voltage.

516 Our novel method generated measurable and physiologically meaningful spatial effects. Fitting the model
517 to the data yielded an estimate of electrotonic length of SNr dendrites of 0.4 mm, which is of the correct
518 order of magnitude and consistent with the diameter of the dendrites (47). In addition, the optogenetic
519 stimulation we employ consists of illuminating an entire portion of the dendritic field, beginning at and
520 including the soma. The spatial effects that we detect using this method are robust but small.
521 Interestingly, our theoretical model of the dendrite predicts that the spatial effect induced by a localized
522 input would be significantly more dramatic (Fig. 1B). This calls for a further investigation of the effect of
523 the dendritic electrotonic structure using localized stimulation, which takes into account the structure of
524 each specific dendritic tree.

525 The stimulation conditions that we employ could also be physiologically relevant. Because GPe targets
526 the proximal somatic region (38,39,47), while the STN targets the entire dendritic tree uniformly (36,37),
527 the proximal illumination could reflect a coherent activation of afferent GPe inputs, while the full-field
528 illumination could reflect the coherent activation of afferent STN inputs. Coherent rhythmic input could
529 impinge on SNr neurons both under physiological, such as sleep (44) or anesthesia (16,18), and
530 pathophysiological conditions, such as parkinsonism (45). Thus, the spatial effect that we demonstrate
531 could provide insight into how rhythmic pallidal and STN inputs may interact to drive and entrain SNr
532 neurons, and possibly drive pathological oscillatory activity in Parkinson's disease (PD) (60). An
533 interesting future direction would thus be to further examine the physiological significance of our
534 findings by optogenetically activating natural afferents to SNr cells arising from the GPe, the STN and
535 the striatum both *in vitro* and *in vivo.*

536 *Reduced single neuron dynamics and population responses*

537 A fundamental question in the field of neuroscience is how the properties of the single cell manifest
538 themselves in a network of neurons. Both theoretical and experimental work have demonstrated that the
539 large scale network dynamics of neurons often depend on a simple dynamical property or
540 characterization of the individual neurons, rather than their high-dimensional and morphologically
541 complex description. For example, a large body of work, conducted over the past decade by Wolf and
542 collaborators, has shown that the high-fidelity of the population rate response of cortical neurons arises
543 from and depends on the rapidity of action potential initiation. Because cortical neuronal dynamics are
544 governed by a balance between excitation and inhibition that keeps these neurons near threshold, when
545 an abrupt change occurs in their shared input, sufficiently many neurons can cross threshold and follow
546 the input. Therefore, the only rate limiting factor, in these fluctuation driven neurons, is how fast each
547 one can generate an action potential (51,61,62).

548 This mechanism of stochastic resonance provides a good description of population responses in the
549 cortex, the hippocampus and many other brain regions. However, in the BG, many neurons are not driven
550 by noise but rather by their autonomous pacemaking. In this case, the framework for simplifying the
551 description of neurons is the phase reduction method (19,21,58) where each neuron is characterized by its
552 mean intrinsic rate and its PRC. Here too the high-fidelity of the population response can be derived from
553 the PRC (50,51). It turns out that the limiting factor on the fidelity of the response is the final descending
554 part of the PRC. The initial rising phase of the PSTH, which is a reflection of the rapidity with which the
555 population can respond, scales like the intrinsic period of the pacemaker and is roughly a mirror image of
556 the final descending region of the PRC (see eq. 3). Unlike in the case of fluctuation driven neurons, the
557 pacemakers whose phase is closest to action potential threshold are the least responsive to input (the PRC
558 vanishes there) and therefore cannot contribute to the population response. In order for populations of
559 pacemakers to attain a high fidelity representation of their input they need to discharge faster. In primates
560 and humans, SNr GABAergic cells exhibit very high discharge rates of up to 145 spikes/s (63), enabling
561 SNr projection neurons to transmit information rapidly.

562 *Spiking resonances in SNr determine their entrainability*

563 According to our analysis, SNr GABAergic cells and their dendrites are linear and do not exhibit
564 subthreshold resonances. However, they do display spiking resonances - the firing of SNr pacemakers
565 can be entrained to rhythmic inputs, if the stimulation frequency is close enough to the neuron's intrinsic
566 frequency – its natural discharge rate. We demonstrated this first using periodic somatic current injection.
567 We then incorporated optogenetic stimulation into this scheme and demonstrated that the tendency of the
568 SNr cells to be entrained to rhythmic inputs is significantly affected by the dendrite, with inputs arriving
569 at different locations inducing distinct phases of locking. The spiking resonance acts as a filter - signals
570 containing frequencies near the natural discharge frequency of the neuron will be transmitted more
571 effectively (52,64,65). It is therefore possible that deep brain stimulation is only therapeutically effective

572 at frequencies in the 120-140 Hz range (66), because it needs to successfully entrain BG output neurons
573 (e.g., SNr) whose spiking resonances are in that range due to these pacemakers' exceptionally high
574 intrinsic firing rates (63).

575 *Impact of dendritic structure on populations responses*

576 A recent theoretical study has argued that the impedance load of the dendritic arbor should affect the
577 rapidness of spike initiation (67), which should invariably impact the response fidelity of fluctuation
578 driven neurons such as pyramidal neurons. Similarly, but in the case of pacemakers, our study
579 demonstrated that dendrites affect two aspects of the collective dynamics of SNr GABAergic
580 pacemakers. First, we examined the fidelity of the population rate response and showed that the peak in
581 the response induced by a stimulation of the entire dendritic arbor is delayed compared to stimulation of
582 the soma and proximal dendrites. Next, we showed that when the firing of an autonomously active
583 neuron is entrained by a periodic input, locking tends to occur at a later effective phase for activation of a
584 larger portion of the dendritic arbor. Importantly, our study of the dendritic impact on currents arriving at
585 the soma allowed us to relate – for the first time empirically – these population effects to the transmission
586 properties of SNr dendrites. Because SNr neurons are actively decorrelated by recurrent connections
587 (44,68) they are perfectly fit to function as a population readout of the integrated activity of the direct and
588 indirect pathways. Thus, the rapidity and fidelity of transmission in SNr projection neurons are highly
589 important.

590 *Implications of SNr dendritic delays on the race between go and stop signals*

591 The intracellular response latency of SNr GABAergic cells is typically attributed to synaptic delays
592 (5,12). However, our results suggest that the delay in the response of a population of neurons can
593 originate from additional sources. We show, as previously suggested (50), that the fidelity of response in

a population of oscillating neurons is determined by the shape of their PRCs, and that the PRC is in turn affected by the dendrite. The earlier peak in the response to proximal inputs, implies that inputs arising from the GPe, belonging to the indirect pathway, would generate a faster response than inputs originating from direct pathway striatal spiny projection neurons. STN projections onto SNr neurons are distributed along the entire length of the dendrite, and would thus induce a delay that is longer than that generated by proximal GPe inputs, but considerably shorter than the delay in response to distal striatal inputs.

The decision to interrupt and cancel actions is widely viewed as a core function of BG circuits (69–71). According to this view, output neurons of the BG, such as SNr GABAergic neurons, are the final common target of a race between two competing signals: a ‘go’ signal transmitted by the direct pathway dSPNs, which are thought to promote movement by inhibiting SNr neurons; and a ‘stop’ signal transmitted via indirect pathway STN neurons that block behavior by exciting the same SNr neurons. Evidence of this race was observed in the peristimulus time histograms (PSTHs) of SNr and STN neurons (17). However, because the go signal is a monosynaptic input whereas the stop signal is a polysynaptic input, the go signal would have an inherent advantage in the race to activate or entrain SNr neurons. Here we show that dendritic delays are manifested in the PSTH rise time in SNr pacemakers, and thus have a direct impact on the relative timing between the two competing signals. This may act as a compensation mechanism, effectively delaying direct pathway inputs originating from the striatum so that they impinge on the axosomatic region of the SNr neuron together with the indirect pathway inputs that coursed through the polysynaptic route via the STN, enabling a fair competition between go and stop signals.

614

Materials and Methods

615

Animals

616

This study was carried out in accordance with the recommendations of and approved by the Hebrew 617 University Animal Care and Use Committee. Experiments were conducted with 3-12-week old male and 618 female homozygous transgenic Thy1-ChR2 mice [B6.Cg-Tg (Thy1-COP4/EYFP) 18Gfng/1]. These mice 619 express ChR2 under the Thy1 promoter (42) in SNr GABAergic neurons. In SNr GABAergic cells, ChR2 620 is expressed in the soma as well as all parts of the dendritic field (43).

621

Slice preparation

622

Mice were deeply anesthetized with ketamine (200 mg/kg)–xylazine (23.32 mg/kg) and perfused 623 transcardially with ice-cold-modified artificial cerebrospinal fluid (ACSF) bubbled with 95% O2–5% 624 CO2, and containing (in mM) 2.5 KCl, 26 NaHCO3, 1.25 Na2HPO4, 0.5 CaCl2, 10 MgSO4, 0.4 ascorbic 625 acid, 10 glucose and 210 sucrose. The brain was removed, and 240 μm thick sagittal slices containing the 626 SNr were cut in ice-cold-modified ACSF. Slices were then submerged in ACSF, bubbled with 95% 627 O2–5% CO2, containing (in mM) 2.5 KCl, 126 NaCl, 26 NaHCO3, 1.25 Na2HPO4, 2 CaCl2, 2 MgSO4 628 and 10 glucose, and stored at room temperature for at least 1 h prior to recording.

629

Electrophysiological recording

630

The slices were transferred to the recording chamber mounted on a Zeiss Axioskop fixed-stage 631 microscope and perfused with oxygenated ACSF at 31ºC. To guarantee that the effects we measured were 632 generated post-synaptically, the ACSF solution contained 10 μ*M* 6,7-Dinitroquinoxaline-2,3-dione 633 (DNQX) to block AMPA receptors, 50 μ*M* D-(-)-2-Amino-5-phosphonopentanoic acid (D-AP5) to block

634 NMDA receptors, 10 μM 6-Imino-3-(4-methoxyphenyl)-1(6*H*)-pyridazinebutanoic acid hydrobromide
635 (SR) to block $GABA_A$ receptors, and 2 μM
636 (2*S*)-3-[[(1*S*)-1-(3,4-Dichlorophenyl)ethyl]amino-2-hydroxypropyl] (phenylmethyl)phosphinic acid
637 hydrochloride (CGP) to block $GABA_B$ receptors. An Olympus 60X, 0.9 NA water-immersion objective
638 with a 26.5 mm field number (FN) was used to examine the slice using standard infrared differential
639 interference contrast video microscopy. Patch pipette resistance was typically 4-5 MΩ when filled with
640 recording solutions. For both whole-cell and cell-attached recordings the intracellular solution contained
641 (in mM) 135.5 KCH3SO3, 5 KCl, 2.5 NaCl, 5 Na-phosphocreatine, 10 HEPES, 0.2 EGTA, 0.21
642 Na2GTP, and 2 Mg1.5ATP, pH 7.3 with KOH (280–290 mOsm/kg). For perforated patch recordings 2
643 $\mu g/ml$ of gramicidin B was added to the intracellular solution. In whole-cell voltage clamp recordings,
644 cells were held between -70 to -80mV to avoid spiking, or at -50mV and -60mV to search for possible
645 voltage dependencies in the subthreshold range. In cell-attached and perforated patch current clamp
646 recordings, neurons discharged spontaneously, and figures depict the temporal derivative of the voltage.
647 Electrophysiological recordings were obtained with a MultiClamp 700B amplifier (Molecular Devices,
648 Sunnyvale, CA). Signals were filtered at 10 kHz online, digitized at 20 kHz and logged onto a personal
649 computer with the Signal 6 software (Cambridge Electronic Design, Cambridge, UK).

650 *Optogenetic stimulation*

651 Optogenetic stimulation was achieved with blue-light (470 nm) LED illumination via the objective
652 (Mightex, Toronto, ON, Canada). Field illumination was applied under two conditions, in all experiments
653 conducted in this study: a) proximal stimulation illuminating a ~40 μm diameter around the soma
654 (achieved by placing an opaque disk with a central pinhole at the 60X objective's rear focal plane),
655 thereby targeting the soma and proximal dendrites (proximal); and b) full-field illumination stimulating
656 the entire SNr (and beyond) with a 5X objective which excites the soma and the entire dendritic field

657 (full-field). In all experiments, LED light intensity at the back plane of the objective was chosen such that
658 stimulation generated comparable current and voltage responses for the two conditions.

659 For PRC measurements, cells were recorded in the cell-attached, current clamp mode (to preclude any
660 feedback from the amplifier that can alter the cells firing pattern). Barrages of light pulses were delivered
661 based on a previously described method (43). Pulses were 0.5-1 ms long and were separated by random,
662 exponentially distributed inter-pulse intervals, with means of 6 ms and 2.17 ms (from pulse onset until
663 the onset of the next pulse) for the full-field and proximal illumination conditions, respectively. LED
664 light intensity at the back plane of the objective was 15 mW for proximal illumination through the disk
665 with the pinhole and 0.03-0.06 mW for full-field illumination. Stimulation consisted of 3 seconds of
666 baseline recording followed by 9 seconds of barrage stimulation, and this was repeated 25 times. Each of
667 the 25 repetitions was a different realization of exponentially distributed inter-pulse intervals, but all cells
668 received the same set of stimulation barrages. This stimulus was also used for measurements of ChR2
669 current responses. To avoid the effect of ChR2 deactivation, only data collected during the last 5 seconds
670 of stimulation were used in the analysis.

671 In electrotonic structure experiments, cells were stimulated with a temporal sinusoid at different
672 frequencies (0.25-16 Hz, 3-4 seconds per frequency). LED light intensity at the back plane of the
673 objective was 1.5mW for proximal illumination and 1.5-15 μW for full-field illumination.

674 In entrainment experiments, cells were recorded in the perforated patch configuration and allowed to fire
675 spontaneously as 30-60 second long sinusoidal waveforms at different frequencies around the natural
676 firing frequency of the cell (typically ~7 Hz) were delivered. Stimulation was applied either
677 optogenetically, in the proximal or full-field illumination configurations, or as a current injection with a
678 10-20 pA amplitude. LED light intensity at the back plane of the objective was 0.15-0.9 mW for
679 proximal illumination and 15-30 μW for full-field illumination.

Two-photon laser scanning microscopy (2PLSM)

Neurons were patch clamped with 100 µm Alexa Fluor 568 (Molecular Devices) in the patch pipette. The two-photon excitation source was a Chameleon Vision II tunable Ti:Sapphire pulsed laser (Coherent, Santa Clara, CA, USA) tuned to 820 nm. The images were collected with the Femto2D system (Femtonics, Budapest, Hungary) which includes two 3mm galvo-scanners and a multi-alkaline non-descanned photomultiplier tube for imaging Alexa Fluor. Z stacks of optical sections (spaced 2 µm apart) were collected using 0.2 µm pixels and 15 µs dwell times. The image in Figure 2A is a montage of several collapsed Z stacks.

Data analysis

Data were analyzed and curve fitting was performed using custom made code in MATLAB (MathWorks, Natick, MA, USA).

<u>Electrotonic structure study:</u> Phase shifts between the optogenetic sinusoidal stimulation and the somatic current response were determined by the location of the peak in the cross-correlation function (CCF) between the two traces, for each stimulation frequency and for each illumination condition. We fit these data with the curve we derive in the Results section (eq. 2) from our cable theoretic model and use the fit to estimate the effective time and space constants associated with the dendrites of SNr GABAergic neurons.

<u>PRC estimation:</u> Steady-state data (4-9 seconds after beginning of stimulation) were analyzed as previously described (43,48), with a few minor changes. In short, spikes were detected and each interspike interval (ISI) was divided into 50 equally-sized bins (i.e., for each ISI, the bin size scales with the duration of the ISI), where the *j*th bin corresponds to the phase $\varphi_j = (j - 0.5)/50$. The number of pulses delivered in each bin of each ISI, denoted $p_{\alpha,j}$ (α is the index of the ISI) was counted and the

mean value (averaged over all ISIs and all bins) was subtracted resulting in $\Delta p_{\alpha,j}$. Then, a multiple regression analysis was performed with $\Delta p_{\alpha,j}$ values as the independent variables and ISI_α values as the dependent variables. If we denote the PRC as $Z(\varphi)$, then the regression coefficients $Z(\varphi_j)$ provide a unique solution for the PRC (49). Because the resulting PRCs had a triangular form (43), we fit an acute triangle

to the resulting data points, whose base is the segment from 0 to 1 and whose peak is located at the point $(\theta, 1)$. The same triangle was used for the analysis of the population responses and entrainment of SNr neurons. As discussed presently, we need the Fourier series of this triangle which is given by $\hat{Z}_0 = \frac{1}{2}$ [6] and for all other k

$$\hat{Z}_k = \frac{exp(-2\pi ik\theta)-1}{4\pi^2\theta(1-\theta)k^2} \quad [7]$$

<u>Peristimulus time histogram (PSTH) estimation</u>: Because the barrages of pulses are realizations of a time varying Poisson process, with a step-like onset, the same spiking data were used to perform the population rate response analysis to a step-like perturbation. PSTHs centered around the onset of the barrage stimulus were generated. The width of each bin was 4 ms, and data included 25 repetitions of each of the 19 cells. Given the Fourier series of a neuron's PRC, one can calculate the predicted shape of the neuron's PSTH using the Fokker-Planck formalism (50,51). This calculation yields the following model that we fit to the empirical PSTHs, denoted *R(t)*, corresponding to each of the two stimulation conditions:

$$R(t) = F_{base} + H(t)\,\frac{F_{steady}-F_{base}}{\hat{Z}_0}\sum_{k=-\infty}^{\infty}\hat{Z}_k exp(-\left[\frac{\sigma^2k^2}{2} + i\frac{2\pi k}{T_0}\right]t) \quad [8]$$

Where F_{base} is the cells' average baseline firing rate prior to stimulus onset, F_{steady} is the average steady-state firing rate after relaxation, T_0 is the baseline period ($= \frac{1}{F_{base}}$), and $\hat{Z}_k$ is the kth Fourier coefficient of the PRC (eq.6 and eq.7). *H(t)* is the Heaviside function.

We fit *R(t)* (eq. 8) to the observed baseline and steady-state rates of the PSTH and the structure of the first 50 ms after stimulus onset. The parameters that were estimated were σ and θ, for each stimulation condition, and we used *k* values ranging from -100 to 100.

For ChR2 current response measurements, a double exponent of the form $A(exp(-\frac{t}{\tau_{rise}}) - exp(-\frac{t}{\tau_{decay}}))$ [9] was fit to average current response curves, and the parameter *A* as well as the time constants τ_{rise} and τ_{decay} were extracted (43).

<u>Entrainment to rhythmic inputs:</u> Entrainment of the cell's spiking activity to rhythmic inputs was evaluated based on previously described methods (52). For each spike, the perturbed period T_p was measured as a function of its effective phase ψ - its phase with respect to the period of the rhythmic stimulus. The fitted curve for these measurements (Fourier fit, first 3 modes) was used to generate an iterative map of the effective phase ψ_{n+1} of the next action potential as a function of the effective phase ψ_n of the current action potential (see eq. 3 in Results). Cobweb plotting was applied to this mapping to investigate the dynamics of the evolution of effective phases (52). In order to generate a prediction for phases of locking using proximal and full-field illumination, a differential equation describing the evolution of the cell's intrinsic phase (see eq. 5 in Results) was numerically integrated in XPPAUT (72), using the idealized triangular PRC fit, with the values of θ extracted from the estimate of the PSTH.

The probability distribution of effective phases was used to generate a circular variance vector, which provides a measure of the variation of effective phases (54). The amplitude of the circular variance vector represents the extent to which the firing of the neuron was entrained by the oscillatory input, and its phase indicates the effective phase of entrainment, which corresponds to the peak of the distribution of effective phases. Each cell was stimulated with temporal sine waveforms at several different frequencies (2.5-21 Hz), and a circular variance vector was estimated for each trial. In order to investigate phases of entrainment, we only included instances where the amplitude of the circular variance was larger than 0.175. This threshold represents the 95th percentile in the distribution of the amplitude of circular

variances achieved by bootstrapping. The surrogate data were series of 100 uniformly distributed random numbers (between 0 and 1), because our entrainement experiments typically included on the order of 100 ISIs.

Statistics: The nonparametric two-tailed Wilcoxon rank-sum test (RST) was used for non-matched samples, and that nonparametric Wilcoxon signed-rank test (SRT) was used for matched samples. Error bars represent standard errors of the mean. The parametric ANCOVA test was used to test significant changes in curves. In PRC analysis the test was applied to the rise stage of the curves. Null hypotheses were rejected if the P-value was below 0.05.

Acknowledgments

Eng. Anatoly Shapochnikov provided excellent technical support. This work was funded by a European Research Council (ERC) Consolidator Grant (no. 646886) to J.A.G.

Author Contribution

L.T. conceptualized, designed and conducted the experiments, analyzed the data, developed the theory and conducted simulations and wrote the paper. J.A.G. conceptualized, designed and supervised the experiments, developed the theory and conducted simulations, wrote the paper, secured funding and is responsible for the content of the manuscript.

Declaration of Interests

That authors declare no competing interests.

766 **References**

767 1. Anderson M, Yoshida M. Electrophysiological evidence for branching nigral projections to the
768 thalamus and the superior colliculus. Brain Res. 1977 Dec 2;137(2):361–4.

769 2. Anderson ME, Yoshida M. Axonal branching patterns and location of nigrothalamic and
770 nigrocollicular neurons in the cat. J Neurophysiol. 1980 Apr;43(4):883–95.

771 3. Niijima K, Yoshida M. Electrophysiological evidence for branching nigral projections to pontine
772 reticular formation, superior colliculus and thalamus. Brain Res. 1982 May 6;239(1):279–82.

773 4. Dray A, Gonye TJ, Oakley NR. Caudate stimulation and substantia nigra activity in the rat. J
774 Physiol. 1976 Aug;259(3):825–49.

775 5. Deniau JM, Menetrey A, Charpier S. The lamellar organization of the rat substantia nigra pars
776 reticulata: segregated patterns of striatal afferents and relationship to the topography of
777 corticostriatal projections. Neuroscience. 1996 Aug;73(3):761–81.

778 6. McBride RL, Larsen KD. Projections of the feline globus pallidus. Brain Res. 1980 May
779 5;189(1):3–14.

780 7. Bevan MD, Smith AD, Bolam JP. The substantia nigra as a site of synaptic integration of
781 functionally diverse information arising from the ventral pallidum and the globus pallidus in the rat.
782 Neuroscience. 1996 Nov;75(1):5–12.

783 8. Parent A, Hazrati L-N. Functional anatomy of the basal ganglia. II. The place of subthalamic
784 nucleus and external pallidum in basal ganglia circuitry. Brain Res Rev. 1995;20(1):128–54.

785 9. Smith Y, Bevan MD, Shink E, Bolam JP. Microcircuitry of the direct and indirect pathways of the
786 basal ganglia. Neuroscience. 1998 Sep;86(2):353–87.

787 10. Kang Y, Kitai ST. Electrophysiological properties of pedunculopontine neurons and their

postsynaptic responses following stimulation of substantia nigra reticulata. Brain Res. 1990 Dec 3;535(1):79–95.

11. Naito A, Kita H. The cortico-nigral projection in the rat: an anterograde tracing study with biotinylated dextran amine. Brain Res. 1994;637(1-2):317–22.

12. Nakanishi H, Kita H, Kitai ST. Intracellular study of rat substantia nigra pars reticulata neurons in an in vitro slice preparation: electrical membrane properties and response characteristics to subthalamic stimulation. Brain Res. 1987 Dec 22;437(1):45–55.

13. Atherton JF, Bevan MD. Ionic mechanisms underlying autonomous action potential generation in the somata and dendrites of GABAergic substantia nigra pars reticulata neurons in vitro. J Neurosci. 2005 Sep 7;25(36):8272–81.

14. Lutas A, Birnbaumer L, Yellen G. Metabolism regulates the spontaneous firing of substantia nigra pars reticulata neurons via KATP and nonselective cation channels. J Neurosci. 2014 Dec 3;34(49):16336–47.

15. Lutas A, Lahmann C, Soumillon M, Yellen G. The leak channel NALCN controls tonic firing and glycolytic sensitivity of substantia nigra pars reticulata neurons. Elife [Internet]. 2016 May 13;5. Available from: http://dx.doi.org/10.7554/eLife.15271

16. Magill PJ, Sharott A, Bolam JP, Brown P. Brain state-dependency of coherent oscillatory activity in the cerebral cortex and basal ganglia of the rat. J Neurophysiol. 2004 Oct;92(4):2122–36.

17. Schmidt R, Leventhal DK, Mallet N, Chen F, Berke JD. Canceling actions involves a race between basal ganglia pathways. Nat Neurosci. 2013 Aug;16(8):1118–24.

18. Lobb CJ, Jaeger D. Bursting activity of substantia nigra pars reticulata neurons in mouse parkinsonism in awake and anesthetized states. Neurobiol Dis. 2015 Mar;75:177–85.

19. Kuramoto Y. Chemical Oscillations, Waves, and Turbulence. 1984.

20. Hansel D, Mato G, Meunier C. Synchrony in excitatory neural networks. Neural Comput. 1995 Mar;7(2):307–37.

21. Ermentrout B. Type I membranes, phase resetting curves, and synchrony. Neural Comput. 1996 Jul 1;8(5):979–1001.

22. Ermentrout GB, Kleinfeld D. Traveling electrical waves in cortex: insights from phase dynamics and speculation on a computational role. Neuron. 2001 Jan;29(1):33–44.

23. Pinsker HM. Aplysia bursting neurons as endogenous oscillators. I. Phase-response curves for pulsed inhibitory synaptic input. J Neurophysiol. 1977 May;40(3):527–43.

24. Reyes AD, Fetz EE. Effects of transient depolarizing potentials on the firing rate of cat neocortical neurons. J Neurophysiol. 1993;69(5):1673–83.

25. Bennett BD, Wilson CJ. Synaptic regulation of action potential timing in neostriatal cholinergic interneurons. J Neurosci. 1998 Oct 15;18(20):8539–49.

26. Keck T, Netoff TI, White JA. Responses of CA1 pyramidal neurons: comparing the effects of dendritic and somatic inputs. In: IEEE 30th Annual Northeast Bioengineering Conference, 2004 Proceedings of the [Internet]. 2004. Available from: http://dx.doi.org/10.1109/nebc.2004.1299965

27. Galán RF, Ermentrout GB, Urban NN. Efficient estimation of phase-resetting curves in real neurons and its significance for neural-network modeling. Phys Rev Lett. 2005 Apr 22;94(15):158101.

28. Netoff TI, Acker CD, Bettencourt JC, White JA. Beyond two-cell networks: experimental measurement of neuronal responses to multiple synaptic inputs. J Comput Neurosci. 2005 Jun;18(3):287–95.

29. Farries MA, Wilson CJ. Phase response curves of subthalamic neurons measured with synaptic input

and current injection. J Neurophysiol. 2012 Oct;108(7):1822–37.

30. Goldberg JA, Atherton JF, Surmeier DJ. Spectral reconstruction of phase response curves reveals the synchronization properties of mouse globus pallidus neurons. J Neurophysiol. 2013 Nov;110(10):2497–506.

31. Crook SM, Ermentrout GB, Bower JM. Dendritic and synaptic effects in systems of coupled cortical oscillators. J Comput Neurosci. 1998 Jul;5(3):315–29.

32. Goldberg JA, Deister CA, Wilson CJ. Response properties and synchronization of rhythmically firing dendritic neurons. J Neurophysiol. 2007 Jan;97(1):208–19.

33. Remme MWH, Rinzel J. Role of active dendritic conductances in subthreshold input integration. J Comput Neurosci. 2011 Aug;31(1):13–30.

34. Grofova I, Deniau JM, Kitai ST. Morphology of the substantia nigra pars reticulata projection neurons intracellularly labeled with HRP. J Comp Neurol. 1982 Jul 10;208(4):352–68.

35. Mailly P, Charpier S, Mahon S, Menetrey A, Thierry AM, Glowinski J, et al. Dendritic arborizations of the rat substantia nigra pars reticulata neurons: spatial organization and relation to the lamellar compartmentation of striato-nigral projections. J Neurosci. 2001 Sep 1;21(17):6874–88.

36. Rinvik E, Ottersen OP. Terminals of subthalamonigral fibres are enriched with glutamate-like immunoreactivity: an electron microscopic, immunogold analysis in the cat. J Chem Neuroanat. 1993 Jan;6(1):19–30.

37. Bevan MD, Bolam JP, Crossman AR. Convergent synaptic input from the neostriatum and the subthalamus onto identified nigrothalamic neurons in the rat. Eur J Neurosci. 1994 Mar 1;6(3):320–34.

38. Totterdell S, Bolam JP, Smith AD. Characterization of pallidonigral neurons in the rat by a

854 combination of Golgi impregnation and retrograde transport of horseradish peroxidase: their
855 monosynaptic input from the neostriatum. J Neurocytol. 1984 Aug;13(4):593–616.

856 39. Smith Y, Bolam JP. Neurons of the substantia nigra reticulata receive a dense GABA-containing
857 input from the globus pallidus in the rat. Brain Res. 1989 Jul 24;493(1):160–7.

858 40. Smith Y, Bolam JP. The output neurones and the dopaminergic neurones of the substantia nigra
859 receive a GABA-Containing input from the globus pallidus in the rat. J Comp Neurol.
860 1990;296(1):47–64.

861 41. von Krosigk M, Smith Y, Bolam JP, Smith AD. Synaptic organization of GABAergic inputs from
862 the striatum and the globus pallidus onto neurons in the substantia nigra and retrorubral field which
863 project to the medullary reticular formation. Neuroscience. 1992 Oct;50(3):531–49.

864 42. Arenkiel BR, Peca J, Davison IG, Feliciano C, Deisseroth K, Augustine GJ, et al. In vivo
865 light-induced activation of neural circuitry in transgenic mice expressing channelrhodopsin-2.
866 Neuron. 2007 Apr 19;54(2):205–18.

867 43. Higgs MH, Wilson CJ. Measurement of phase resetting curves using optogenetic barrage stimuli. J
868 Neurosci Methods. 2017 Sep 1;289:23–30.

869 44. Mizrahi-Kliger AD, Kaplan A, Israel Z, Bergman H. Desynchronization of slow oscillations in the
870 basal ganglia during natural sleep. Proc Natl Acad Sci U S A. 2018 May 1;115(18):E4274–83.

871 45. Brazhnik E, Cruz AV, Avila I, Wahba MI, Novikov N, Ilieva NM, et al. State-dependent spike and
872 local field synchronization between motor cortex and substantia nigra in hemiparkinsonian rats. J
873 Neurosci. 2012 Jun 6;32(23):7869–80.

874 46. Rall W. Electrophysiology of a Dendritic Neuron Model. Biophys J. 1962;2(2):145–67.

875 47. Koch C. Biophysics of Computation: Information Processing in Single Neurons. Oxford University

Press; 2004. 562 p.

48. Wilson CJ, Barraza D, Troyer T, Farries MA. Predicting the responses of repetitively firing neurons to current noise. PLoS Comput Biol. 2014 May;10(5):e1003612.

49. Netoff T, Schwemmer MA, Lewis TJ. Experimentally Estimating Phase Response Curves of Neurons: Theoretical and Practical Issues. In: Phase Response Curves in Neuroscience. 2011. p. 95–129.

50. Schleimer J-H, Stemmler M. Coding of information in limit cycle oscillators. Phys Rev Lett. 2009 Dec 11;103(24):248105.

51. Touzel M, Wolf F. Complete Firing-Rate Response of Neurons with Complex Intrinsic Dynamics. PLoS Comput Biol. 2015 Dec;11(12):e1004636.

52. Wilson CJ. Predicting the response of striatal spiny neurons to sinusoidal input. J Neurophysiol. 2017 Aug 1;118(2):855–73.

53. Wilson CJ, Beverlin B 2nd, Netoff T. Chaotic desynchronization as the therapeutic mechanism of deep brain stimulation. Front Syst Neurosci. 2011 Jun 21;5:50.

54. Fisher NI. Statistical Analysis of Circular Data. 1993.

55. Bower JM. Constructing New Models. In: The Book of GENESIS. 1998. p. 195–201.

56. Herz AVM, Gollisch T, Machens CK, Jaeger D. Modeling single-neuron dynamics and computations: a balance of detail and abstraction. Science. 2006 Oct 6;314(5796):80–5.

57. Prinz AA, Billimoria CP, Marder E. Alternative to hand-tuning conductance-based models: construction and analysis of databases of model neurons. J Neurophysiol. 2003 Dec;90(6):3998–4015.

58. Winfree AT. The Timing of Biological Clocks. Macmillan; 1987. 199 p.

59. Williams TL, Bowtell G. The calculation of frequency-shift functions for chains of coupled oscillators, with application to a network model of the lamprey locomotor pattern generator. J Comput Neurosci. 1997 Jan;4(1):47–55.

60. Plenz D, Kital ST. A basal ganglia pacemaker formed by the subthalamic nucleus and external globus pallidus. Nature. 1999 Aug 12;400(6745):677–82.

61. Naundorf B, Wolf F, Volgushev M. Unique features of action potential initiation in cortical neurons. Nature. 2006 Apr 20;440(7087):1060–3.

62. Tchumatchenko T, Malyshev A, Wolf F, Volgushev M. Ultrafast population encoding by cortical neurons. J Neurosci. 2011 Aug 24;31(34):12171–9.

63. Schultz W. Activity of pars reticulata neurons of monkey substantia nigra in relation to motor, sensory, and complex events. J Neurophysiol. 1986;55(4):660–77.

64. Hunter JD, Milton JG, Thomas PJ, Cowan JD. Resonance effect for neural spike time reliability. J Neurophysiol. 1998 Sep;80(3):1427–38.

65. Schreiber S, Samengo I, Herz AVM. Two distinct mechanisms shape the reliability of neural responses. J Neurophysiol. 2009 May;101(5):2239–51.

66. Moro E, Esselink RJA, Xie J, Hommel M, Benabid AL, Pollak P. The impact on Parkinson's disease of electrical parameter settings in STN stimulation. Neurology. 2002 Sep 10;59(5):706–13.

67. Eyal G, Mansvelder HD, de Kock CPJ, Segev I. Dendrites impact the encoding capabilities of the axon. J Neurosci. 2014 Jun 11;34(24):8063–71.

68. Higgs MH, Wilson CJ. Unitary synaptic connections among substantia nigra pars reticulata neurons.

J Neurophysiol. 2016 Jun 1;115(6):2814–29.

69. Jahfari S. On the impact of individual differences between key nodes of response inhibition [Internet]. PsycEXTRA Dataset. 2011. Available from: http://dx.doi.org/10.1037/e512592013-085

70. Baunez C, Humby T, Eagle DM, Ryan LJ, Dunnett SB, Robbins TW. Effects of STN lesions on simple vs choice reaction time tasks in the rat: preserved motor readiness, but impaired response selection. Eur J Neurosci. 2001 Apr;13(8):1609–16.

71. Eagle DM, Baunez C, Hutcheson DM, Lehmann O, Shah AP, Robbins TW. Stop-signal reaction-time task performance: role of prefrontal cortex and subthalamic nucleus. Cereb Cortex. 2008 Jan;18(1):178–88.

72. Ermentrout B. Simulating, Analyzing, and Animating Dynamical Systems: A Guide to XPPAUT for Researchers and Students. SIAM; 2002. 290 p.